Special Collection: Materials and Technologies for Bioimaging and Biosensing

Shupeng Ning <sup>(1)</sup>; Hao-Chen Chang; Kang-Chieh Fan; Po-Yu Hsiao <sup>(1)</sup>; Chenghao Feng <sup>(1)</sup>; Devan Shoemaker <sup>(1)</sup>; Ray T. Chen <sup>(1)</sup>

Check for updates

Appl. Phys. Rev. 10, 021410 (2023) https://doi.org/10.1063/5.0146079

CrossMark

View Export Online Citation





# 

Cite as: Appl. Phys. Rev. 10, 021410 (2023); doi: 10.1063/5.0146079

Submitted: 9 February 2023 · Accepted: 5 May 2023 ·

Published Online: 25 May 2023







#### **AFFILIATIONS**

- <sup>1</sup>Department of Electrical and Computer Engineering, The University of Texas at Austin, Austin, Texas 78758, USA
- <sup>2</sup>Omega Optics, Inc., 8500 Shoal Creek Blvd., Austin, Texas 78757, USA

Note: This paper is part of the APR Special Topic on Materials and Technologies for Bioimaging and Biosensing.

a)Author to whom correspondence should be addressed: chenrt@austin.utexas.edu

#### **ABSTRACT**

In the context of continued spread of coronavirus disease 2019 (COVID-19) caused by SARS-CoV-2 and the emergence of new variants, the demand for rapid, accurate, and frequent detection is increasing. Moreover, the new predominant strain, Omicron variant, manifests more similar clinical features to those of other common respiratory infections. The concurrent detection of multiple potential pathogens helps distinguish SARS-CoV-2 infection from other diseases with overlapping symptoms, which is significant for providing tailored treatment to patients and containing the outbreak. Here, we report a lab-on-a-chip biosensing platform for SARS-CoV-2 detection based on the subwavelength grating micro-ring resonator. The sensing surface is functionalized by specific antibody against SARS-CoV-2 spike protein, which could produce redshifts of resonant peaks by antigen—antibody combination, thus achieving quantitative detection. Additionally, the sensor chip is integrated with a microfluidic chip featuring an anti-backflow Y-shaped structure that enables the concurrent detection of two analytes. In this study, we realized the detection and differentiation of COVID-19 and influenza A H1N1. Experimental results indicate that the limit of detection of our device reaches 100 fg/ml (1.31 fM) within 15 min detecting time, and cross-reactivity tests manifest the specificity of the optical diagnostic assay. Furthermore, the integrated packaging and streamlined workflow facilitate its use for clinical applications. Thus, the biosensing platform presents a promising approach for attaining highly sensitive, selective, multiplexed, and quantitative point-of-care diagnosis and distinction between COVID-19 and influenza.

Published under an exclusive license by AIP Publishing. https://doi.org/10.1063/5.0146079

#### I. INTRODUCTION

Since the novel coronavirus disease 2019 (COVID-19) caused by severe acute respiratory syndrome coronavirus 2 (SARS-CoV-2) was reported in late 2019, the world is continuously threatened by the potentially fatal infectious disease. <sup>1,2</sup> The highly contagious virus quickly spread to most continents within a few weeks and has infected more than 620 million people, including 6.5 million deaths by November 2022. <sup>3,4</sup> During the COVID-19 pandemic, genetic variants of SARS-CoV-2 are constantly emerging and spreading as new epidemic strains. <sup>5,6</sup> Despite the tremendous advances in epidemiological studies and vaccine developments curbing the progress of epidemic, the variant viruses are more contagious and may generate immune

escape from innate or acquired immune responses, resulting in continued transmission around the world. The early diagnosis of suspected cases is still regarded as the best viable solution to slow down the pandemic without guaranteed preventive measures.

The Omicron variant was officially named by the WHO on November 26, 2021 and quickly replaced the Delta variant as the predominant strain. Compared with previous variants, Omicron has lower disease severity, hospitalization, and death rates. On the other hand, COVID-19 has become more atypical due to the mild symptoms of Omicron, thus difficult to distinguish from other infectious diseases with similar symptoms. Among common respiratory infections, influenza presents many overlapping clinical

manifestations with COVID-19, including fever, cough, sore throat, headache, fatigue, and myalgia.  $^{15,16}$  However, the basic reproduction number ( $R_0$ ) of COVID-19 (9.5 for Omicron) is much higher than influenza (0.9–2.1), which means that the SARS-CoV-2 virus is more contagious.  $^{15,17}$  Hence, timely detection is significant for patients to receive tailored treatment and curbing the epidemic, considering the long-term co-existing of COVID-19 and other respiratory infectious diseases with overlapping symptoms.

In clinical practice, the primary method for COVID-19 diagnosis relies on real-time reverse transcription-polymerase chain reaction (RT-PCR). PCR-based detection shows high accuracy even in the early stages of infection, which makes it the "gold standard" in diagnosis. 18 However, RT-PCR needs advanced laboratories, expensive equipment, and medically trained personnel. In addition, the RT-PCR assay, which involves amplification of viral RNA, can be a time-consuming process that may result in delays in diagnosis. 19,20 Because of the increasing demand for testing and the difficulty of large-scale RT-PCR testing, reliable and rapid diagnostic methods for COVID-19 are necessary. To overcome the challenges, some lab-on-a-chip (LOC) platforms for point-of-care (POC) COVID-19 diagnosis have been developed. 9,21-23 Due to short detection time, convenient operation, and low sample requirements, these LOC techniques show great potential in clinical applications. Among these reported techniques, optical biosensors utilize the change of optical properties resulting from photon-matter interaction to realize the detection of analytes. Optical sensing shows several advantages in the biomedical scenario, including label-free detection, multiplexing capability, instantaneous measurements, etc. 10,24 In the past decades, the maturity of silicon photonics and photonic integrated circuits (PICs) technology promoted the development of optical sensors.<sup>25</sup> Furthermore, the compatibility with microfluidic systems offers more opportunities for LOC sensing.<sup>26-28</sup> Micro-ring resonators have been extensively investigated in PIC biosensors because of high packing density and ease of fabrication.<sup>29-31</sup> However, the limited sensitivity of micro-ring resonator impedes the application in clinical diagnostic assays that require a low limit of detection (LOD). 25,32

In this paper, we demonstrate an optical biosensing platform for the rapid detection of SARS-CoV-2 using subwavelength grating microring resonator (SUMIRR), as shown in Fig. 1. Compared with conventional micro-ring resonator with strip waveguides, the subwavelength grating (SWG) structure [Figs. 1(b) and 1(f)] extends the photon-matter interaction region, thus improving sensitivity. 33-36 The SUMIRRs are functionalized by SARS-CoV-2 spike antibody for the detection of SARS-CoV-2 spikes proteins [Fig. 1(b)]. To address the challenges posed by the untypical and diverse clinical manifestations of new epidemic strains, the LOC sensing platform enables the concurrent detection of another pathogen (influenza A H1N1 in this study) with two parallel detection groups [Fig. 1(c)]. To facilitate operation and improve the reliability of device, we design and fabricate a double-layer microfluidic chip with an anti-backflow Y-shaped structure, which has two operating modes for surface functionalization and concurrent detection, respectively. Additionally, a three-dimensional (3D)-printed holder and specialized photonic packaging are presented to realize system-level integration. In the past few years, various diagnostic assays for COVID-19 were widely available (summarized in Table S1). However, a particularly promising solution, including packaging, testing, and data processing, for POC use that can achieve concurrent quantitative detection of multiple analytes is not yet available. Our SUMIRR-based sensor

detects target SARS-CoV-2 antigen with a conservative LOD of 100 fg/ml (1.31 fM). Furthermore, cross-reactivity tests for SARS-CoV-2 and influenza indicate the specificity of the optical diagnostic assay. The integrated device and auxiliary portable terminal, which offers real-time data processing and the potential to interface with electronic medical records, make the platform promising for POC diagnosis.

# II. DEVICE DESIGN

## A. Design of the sensing platform

In considering the design of a POC platform for quantitative detection, we aimed to develop a device with clinical practicality, high accuracy, and the capacity to integrate with digital systems. Toward this goal, we designed a microfluidic chip that supports dual-channel concurrent detection with a 3D-printing polylactic acid (PLA) chip holder [Figs. 1(d) and 1(e), and S9].

For concurrent detection, two parallel channels need to be placed on the silicon sensing chip with a limited area (5  $\times$  5 mm<sup>2</sup>), and, thus, the microfluidic device was designed as a double-layer structure for reliability and ease of operation [Figs. 1(d) and 2(a)]. As shown in Fig. 2(b), the bottom microfluidic chip was designed with two independent microchannels, and each channel covered three SUMIRRs functioning as a sensing group. In addition, each channel had an inlet and an outlet connected to the top microfluidic chip through via holes. In addition to the left and right ports connected to the two channels in the bottom layer, the top microfluidic chip has a common port connected to both channels. The common port is connected to a special Y-shape anti-counterflow splitter that can operate in two modes. In single-channel mode, the left/right port works as an inlet, while the common port works as outlet. When the sample flows toward downstream (common port) from one branch of the Y-shaped structure, the significant difference in flow resistance of downstream and the other branch will "block" the other branch, thus avoiding the cross-contamination [Figs. 2(c) and 3]. The other mode is the dual-channel mode, where the common port works as inlet, while left port and right port are both outlets. In this mode, the structure is a splitter that bifurcates the upstream fluids toward two sensing groups [Figs. 2(d) and 3]. The anti-counterflow splitter is simulated by the finite element method to optimize chip functionality.<sup>37–39</sup> As shown in Fig. 2(e), the Y-shape structure can avoid counterflow in the single-channel mode without losing the bifurcating function for the dual-channel mode.

For better packaging and integration, we designed a 3D-printed holder. The upper surface of holder is slotted, and the depth equals the thickness of sensing chip (0.75 mm). The slot area is larger than that of sensing chip, which aims to utilize the limited elastic deformation of polydimethylsiloxane (PDMS) to eliminate manufacturing errors from 3D printing while providing enough support for the microfluidic chip. In addition, we designed a comb structure with a height slightly less than slot depth, which serves two purposes. First, the comb structure helps to alignment; meanwhile, the fiber array is fixed on the holder by UV light adhesives, and the comb structure could provide a larger contact area resulting in higher bond strength.

#### B. Design of optical biosensor

The SUMIRR consists of a micro-ring and a bus waveguide constructed by periodic pillars with a period much smaller than the

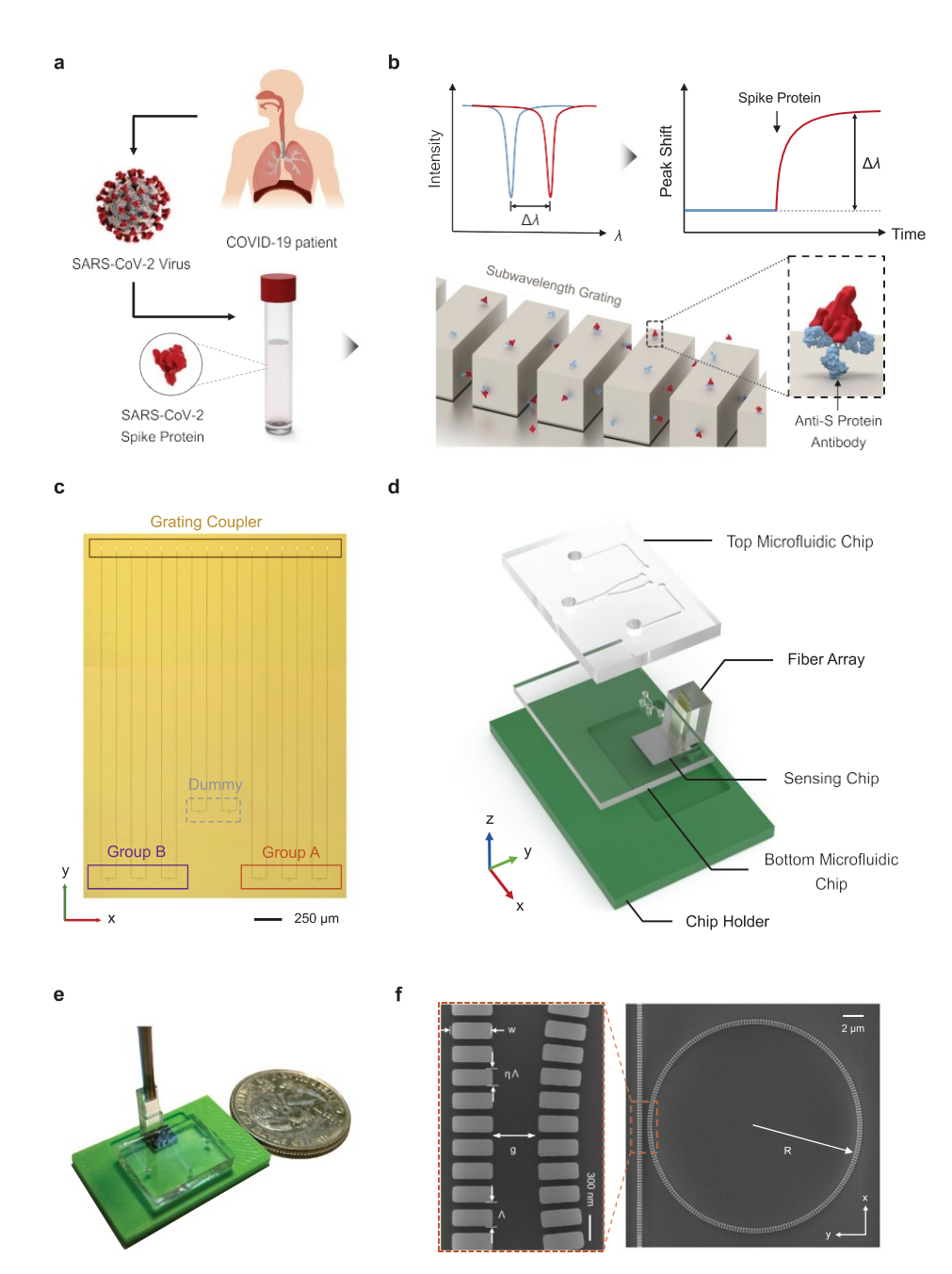


FIG. 1. Working mechanism and design of SUMIRR-based biosensor. (a) SARS-CoV-2 spike protein in phosphate buffered saline (PBS) is the target analyte for the detection. (b) SARS-CoV-2 spike antibodies (blue) are conjugated on SUMIRRs as specific probes. The SUMIRR-based biosensor can quantitatively detect spike protein (red) by tracking the redshift of resonant peaks caused by antigen-antibody combination. (c) Optical micrograph of the silicon sensing chip, which supports concurrent detection of two analytes. There are eight independent sensing channels, each with a pair of grating couplers as input and output. Six channels are divided into two groups for two analytes, while the remaining two channels serve as a dummy group and reference. (d) An exploded view of the LOC biosensing platform. (e) Photograph of the biosensing platform with a quarter dollar for scale. (f) SEM images of the SUMIRR fabricated by E-beam lithography.

operating wavelength.<sup>33,34</sup> One advantage of the subwavelength structure is that the optical properties, including effective index, loss, guiding capabilities, etc., can be modulated by geometric topological designs.<sup>34,35</sup> Importantly, SUMIRRs show good potential for biosensing because the periodic structure increases the effective sensing region, including not only the top and the side of pillars, which leads to more significant photon–matter interaction and higher sensitivity.<sup>40,41</sup>

In this study, SUMIRRs are fabricated on silicon on insulator (SOI) wafers using E-beam lithography. <sup>35,42</sup> Specifically, the silicon pattern sits on the SiO<sub>2</sub> buried layer [Figs. 1(f) and S11], and SUMIRRs are covered by aqueous cladding as sensing units. To ensure

that guided mode exists in SWG waveguides, the effective refractive index of SWG waveguide ( $n_{\rm eff}$ ) must be bigger than the refractive index of bottom buried layer ( $n_{\rm Sio}$ /4 1.45) and cladding layer ( $n_{\rm clad} \approx 1.35$ ). The optimized design shall provide large overlap integral with analytes while maintaining decent waveguide propagation loss. <sup>44</sup> The resonant wavelength  $k_{\rm res}$  can be expressed as

$$k_{\text{res}} \frac{1}{4} \frac{2p \cdot R \cdot n_{\text{eff}}}{m};$$
 (1)

where *R* is the radius of micro-ring and *m* is a positive integer denoting the mode order. In the biosensing scenario, biochemical reactions,

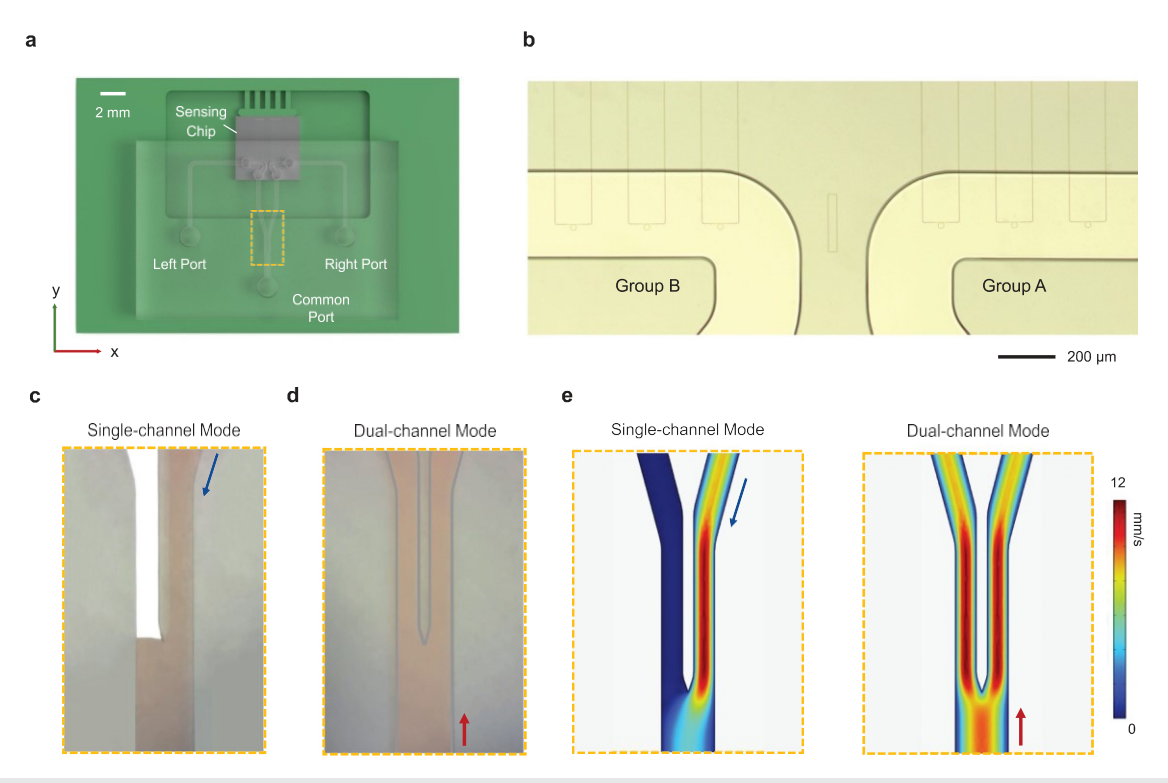


FIG. 2. Overview of microfluidics design. (a) A double-layer PDMS microfluidic chip was designed for dual-channel concurrent detection. Three ports on the top layer serve different functions in different operation modes. (b) The optical micrograph illustrates that the bottom microfluidic chip, bonded on the sensing chip, has two independent channels, and each channel covers three resonators as one sensing group. (c) and (d) The working mechanisms of Y-shape anti-counterflow structure work in two different modes. Red pigment was added to DI water for demonstration purposes. (e) Hydromechanical simulation results display the velocity field distribution of the two modes. In the single-channel mode, the flow rate is 5 *l*/min, and the right port serves as the inlet. In the dual-channel mode, the common port functions as the inlet with a flow rate of 10 *l*/min. Details of the numerical simulation can be found in the supplementary material.

such as antigen–antibody combination and DNA hybridization,  $^{45,46}$  could affect the photon–matter interaction, thus change  $n_{eff}$  according to the Lorentz-Lorenz relation, which manifests in the shift of resonant peaks [Fig. 1(b)].  $^{47}$ 

To evaluate the device's performance, we use quality factor Q and bulk sensitivity  $S_{\text{bulk}}$  to quantify the sensing properties of device. A higher Q means that light has a longer lifetime in the resonator, thus provides stronger interaction with analyte. <sup>40</sup> Q is defined as

# $Q \text{ 1/4 } \mathbf{x}_{\text{res}} \frac{E}{dE = dt} \text{ 1/4 } \frac{2p \cdot n_g}{k_{\text{res}} \cdot a_{\delta m^{-1} \flat}} \approx \frac{k_{\text{res}}}{FWHM}$

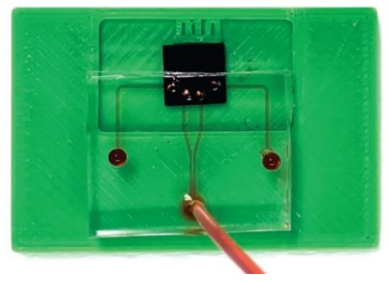
Here,  $x_{res}$  is the resonant frequency, E is the mode's electric field intensity, a represents the total loss in the resonator, and  $n_g$  is the group index of the mode. <sup>48</sup> From the experimental point of view, Q can be approximated by the ratio of  $k_{res}$  to the full width at half maximum (FWHM) bandwidth of resonant peak. <sup>49,50</sup> A higher Q is desirable because of sharper peaks which are easier to detect. The bulk





Flow rate: 5 µL/min

# Dual-channel Mode



Flow rate: 10 µL/min

FIG. 3. Demonstration of microfluidic chip with single-channel and dual-channel mode. Multimedia available online.

sensitivity of SUMIRR  $S_{\text{bulk}}$  was defined as the slope of peak shift vs change in  $n_{\text{clad}}$ , 51 i.e.,

$$S_{\text{bulk}} \frac{1}{4} \frac{Dk_{\text{res}}}{Dn_{\text{clad}}} \frac{k_{\text{res}}}{n_g} \cdot \frac{@n_{\text{eff}}}{@n_{\text{clad}}};$$
 (3)

where  $S_{\text{bulk}}$  is often written as nm/Refractive Index Units (nm/RIU). Considering the influence of Q and  $S_{\text{bulk}}$  on sensing performance, the inherent limit of detection (ILOD) of ring resonator can be defined as follows:<sup>52</sup>

ILOD 
$$\frac{k_{\text{res}}}{Q \cdot S_{\text{bulk}}}$$
: (4)

Taking ILOD as an evaluation criteria, the optimal geometric parameters of SUMIRRs are determined by the full 3D finite difference time domain method (Lumerical FDTD Solutions) and the testing after fabrication. The details of simulation and design parameters are shown in the supplementary material.

# III. MATERIALS AND METHODS

# A. Device fabrication and packaging

The SUMIRR-based sensing chip was custom manufactured by Applied Nanotools Inc. using E-Beam lithography on an SOI wafer with a 220 nm active layer and a 2 lm buried oxide layer (Soitec). Before use, the chip was soaked in piranha for 30 min, followed by deionized (DI) water (W4502, Sigma-Aldrich) and isopropanol (200440, CMC Materials) washing, and then dried under nitrogen (N<sub>2</sub>) stream.

Microfluidic microchannels were fabricated from an SU-8 photoresist (SU-8 2035, Kayaku Advanced Materials) male mold patterned on a 4-in. silicon wafer (71893-07, Electron Microscopy Sciences) using standard soft-lithography processes. The height of microchannel determined by the thickness of SU-8 coating was 50 lm. Microfluidic channels were cast from the male mold with a 10:1 mixture of PDMS base and curing agent (SYLGARD 184 silicone elastomer kit, Dow) and cured at 90 °C for 40 min. The bottom and top layer thicknesses are 3 and 6 mm, respectively. Because of the small chip size, the spacing between two independent microchannels in the bottom layer should be small to ensure sufficient space for packaging. A 240 lm spacing between two 300 lm-width channels showed good stability at a flow rate of  $\leq$  100 ll/min without leakage. The via holes on bottom chip and 3 ports of top layer were punched by 0.75 and 1 mm punchers (PT-T983, Darwin Microfluidics), respectively.

The holder for integration was designed by the CAD software (AutoCAD 2023, Autodesk) and printed by a 3D printer (FLOW, Craftbot) with PLA polymers. After cleaning with IPA and DI water, the bonding surface of sensing chip and PDMS were treated with UV rays in a UV ozone cleaner (T10X10/OES, UVOCS Inc.) for 8 and 5 min, respectively. Then, sensing chip and bottom PDMS were aligned manually according to the pre-designed alignment marks with IPA lubrication and baked in an oven at 90 °C for 1 h. The bonding process for the bottom and top PDMS layers followed the same procedure as the aforementioned step, with the only difference being a UV treatment time of 5 min. For the precise alignments of fibers and grating couplers, the packaging holder and fiber array (pitch 127 lm 8°, Gloriole Electroptic Technology Corp) were anchored to a mechanical stage, as shown in Fig. S1. The input fiber was connected to a broadband LED (DL-BX9-CS5403A, DenseLight), and the output was connected to a C-band optical spectrum analyzer (OM-1C2 MM353,

Optoplex). The position of fiber array is fine-tuned to maximize the output power while still maintaining adequate responses from all channels. Once the optimal position was identified, UV light adhesive glue (37-322, Edmund Optics) was applied to the comb structure of the holder. The assembly was then exposed to UV light overnight to ensure proper curing.

# B. Surface functionalization of micro-ring resonators

The packaging device was exposed to UV rays for 8 min to form hydroxyl groups (-OH) on the SUMIRR surface and remove organic contaminants. A 2% (All concentrations expressed as percentages in this paper are volume ratios.) organosilane reagent (3-aminopropyl) triethoxysilane (APTES), diluted in 95% ethanol solution, was pumped to microfluidic channels via a PTFE tubing (0.6 mm IDx 1 mm OD, Uxcell) at 5 ll/min. The flow rate was controlled by a syringe pump (70-4504, Harvard Apparatus). APTES condensed with-OH results in the formation of siloxane bonds (Si-O-Si) on UV-treated silicon surfaces. 54,55 Notably, it is the oxide layer on Si surface that participates in silanization. The following experiment and related studies confirmed that the natural silicon oxide layer is sufficient for silanization. 48,56-58 The unbounded APTES was removed by 95% ethanol washing at 10 ll/min for 20 min, followed by drying under N<sub>2</sub> stream. Then, the device was baked at 95 °C for 1 h to enhance bonding stability. After silanization, an aqueous solution of 2.5% glutaraldehyde (GA) was introduced at 5 ll/min for 1 h, and then the chip was washed with PBS solution (J61196AP, Thermo Fisher Scientific) at 10 ll/min for 20 min. One aldehyde group binds to the surfaceexpressed -NH2 (from APTES), while the other aldehyde group is available for further cross-linking with the bioreceptor protein. Then, the chip was washed with PBS solution at 10 ll/min for 20 min.

To immobilize the antibody, a 10 lg/mL antibody solution in PBS buffer was introduced for 40 minutes, followed by a 20-min PBS wash. A potential issue with cross-linking by GA is that the aldehyde groups are nonspecific to proteins. Hence, 0.4 mg/ml bovine serum albumin (BSA) was introduced for 20 min to block any unoccupied aldehyde sites, ensuring that the observed peak shift results solely from specific antigen–antibody interactions.<sup>59,60</sup> In this work, we used two antibodies: SARS-CoV-2 spike antibody (40150-D003, Sino Biological, Inc.) and pan influenza A nucleoprotein antibody (40205-R063, Sino Biological, Inc.). Notably, the immobilization for two antibodies was independent. Specifically, the SARS-CoV-2 antibody was introduced from one port (either left port or right port), followed by BSA blocking, while the immobilization of influenza antibody was realized through the other port with the same process. The SARS-CoV-2 antibody with green fluorescence was purchased from Thermo Fisher Scientific (53-6491-82).

#### C. Sample preparation for antigen detection

The SARS-CoV-2 Spike S1-His recombinant protein (40591-V08H, Sino Biological, Inc.) and influenza A H1N1 nucleoprotein (40205-V08B, Sino Biological, Inc.) were diluted in PBS buffer to specific concentrations, depending on experimental requirements.

# D. Sensing measurement

Measurements were conducted on an optical table. The fiber array was connected to a broadband LED and an OSA (alternatively, a

tunable laser and power meter could potentially be used), which communicated with a PC through serial communication. Real-time peak tracking and analysis were accomplished using custom programs (LabView, National Instruments) and algorithms (details can be found in the supplementary material). Plots and histograms were created and analyzed in Origin (Origin 2022, OriginLab).

Optical micrographs and videos were captured on the viewing stage of a microscope (BX51, Olympus) under & magnification. Fluorescent images were obtained using a spinning disk confocal system (CSU-W1, Nikon) and supported by commercial software for analysis.

#### IV. RESULTS

#### A. Bulk sensitivity analysis

Prior to detecting biological samples, we first evaluated the bulk sensitivity of the fabricated SUMIRRs and assessed the sensing performance after packaging. Seven samples, including DI water and six PBS solutions with varying concentrations, were introduced to the device in ascending order of concentration at a flow rate of 10 ll/min. The transmission spectra of SUMIRRs are shown in Fig. 4(a). The free spectral range (FSR) around 1550 nm is 14 nm, and the FWHM of resonant peaks is ~0.93 nm, corresponding to a Q≈1650. According to transmission spectra, the signal amplitude slightly decreases by 0.3 dB/ nm as wavelength increases. Therefore, the resonant peaks near 1535 nm were selected as analytic targets for higher signal-to-noise ratio (SNR). In Fig. 4(b), we took the resonant wavelength with DI water cladding as a baseline and tracked peak shifts in real-time. The relationship between peak shift and refractive index change was plotted and fitted linearly in Fig. 4(c). The results demonstrate that a linear function fits well with a regression correlation coefficient  $R_4^{\circ}0.999$ and the slope, i.e., the bulk sensitivity is 437.2 nm/RIU. The noise level is  $\sim$ 3 pm, and the ILOD is  $\sim$ 2.1 × 10<sup>-3</sup> RIU by Eq. (4).

# B. Detection of SARS-CoV-2 antigen

The viral envelope of SARS-CoV-2 consists of three structural proteins, including membrane protein (M), envelope protein (E), and spike protein (S).<sup>62</sup> The spike protein plays a critical role in penetrating host cells, as it is the primary transmembrane protein.<sup>62,63</sup> Additionally, the spike protein exhibits diversity and specificity among coronaviruses, contributing to the most immune recognition in the

human body. <sup>64</sup> Therefore, the S protein represents an ideal target for the specific detection of SARS-CoV-2. In this study, we utilized the specific combination of S protein and SARS-CoV-2 spike antibody to realize quantitative detection. The antibody used in our research exhibits cross-reactivities with most SARS-CoV-2 variants, including Delta and Omicron. <sup>54</sup> After introducing samples, the antibodies bind to the S proteins, forming antigen—antibody complexes that result in peak shifts.

We developed a protocol for surface functionalization for the diagnostic assay using the SUMIRR-based sensor platform [Fig. 5(a)]. The shift of resonant peak was monitored in real-time throughout the aforementioned process, representing the extent of the reaction. As shown in Fig. 5(b), the trend of peak shift in each step is similar, i.e., with an initial rapid increase followed by a gradual slowdown until it plateaus. To further confirm that the SUMIRR surface was functionalized, we immobilized the SARS-CoV-2 spike antibody with green fluorescence and took fluorescence images for characterization. Figure 5(c) indicates that antibodies with green fluorescent coat uniformly on the waveguide, and the SWG structure exhibits higher fluorescence intensity due to its larger surface area.

To investigate the performance of the SUMIRR-based biosensing platform for COVID-19 detection, we first evaluated the dynamic response of the sensor to varying concentrations of the SARS-CoV-2 spike protein (Fig. 6). Since only one antigen was detected in this section, both the left and right sensing groups served the same function. Consequently, the reagents for surface functionalization were introduced through the common port, divided into two tributaries by a splitter, and directed to the two parallel sensing groups, as illustrated in Fig. S12(a).

We prepared samples with varying concentrations of SARS-CoV-2 spike protein (from 10 pg/ml to 1 lg/ml) and introduced samples successively at a flow rate of 5 ll/min in order of increasing concentration. The response to different samples was monitored in real-time, and the dynamic tracking of peak shift is presented in Fig. 6(a). The stepwise change indicates that the peak shift within the same reaction time exhibits a positive correlation with the antigen concentration. Moreover, the negative control group without antibody coating only shows a slight response [gray line in Fig. 6(a)], indicating that the shift results from antigen–antibody combination rather than a refractive index change caused by increasing concentration. Additionally, the peak shift increases rapidly at the beginning of

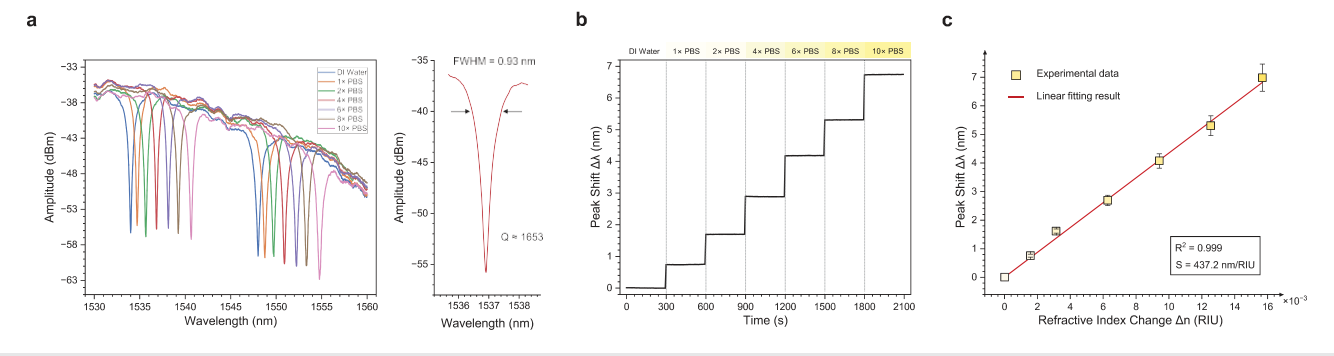


FIG. 4. Bulk sensitivity analysis of the fabricated SUMIRRs. The multiple represents the relative concentration compared with the standard PBS solution. (a) Transmission spectra of SUMIRR in different solutions. (b) Real-time peak shift tracking with increasing solution concentration and refractive index. (c) Linear regression demonstrates a strong linear relationship between peak shift refractive index change and the slope indicates S<sub>bulk</sub>. Details about refractive indexes of PBS solution are provided in Table S5.

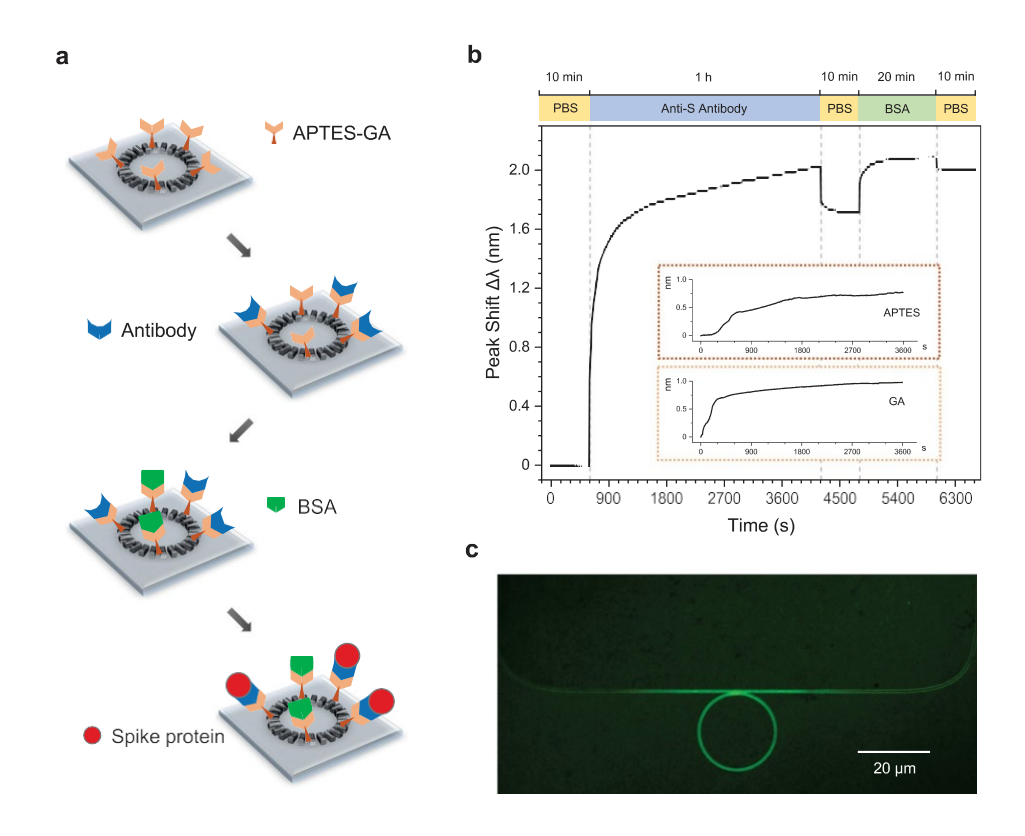


FIG. 5. The surface functionalization of SUMIRRs. (a) Schematic illustrating for surface functionalization and SARS-CoV-2 spike protein detection. (b) Real-time peak shift tracking for the surface functionalization workflow. As the solvents for APTES and GA are ethanol and DI water, respectively, rather than the standard PBS solution used for subsequent reagents, the real-time tracking for APTES/GA coating is depicted separately in the insets with distinct baselines. (c) Fluorescence image of the SUMIRR modified by SARS-CoV-2 spike antibody with green fluorescent.

reaction, and the increase slows down gradually. This general trend, also observed in surface functionalization, implies that the peak shifts over a certain period of time can characterize the extent of antigen—antibody combination, thereby realizing the quantitative detection of the antigen of interest.

After demonstrating the sensing performance of the platform, we further examined the quantitative relationship between peak shift and antigen concentration for clinical detection and explored the LOD of the device. To this end, we prepared samples containing SARS-CoV-2 spike protein ranging from 100 fg/ml to 1 lg/ml. In practical detections, one sensing group can test only one antigen in the sample because the antigen cannot be removed completely once attached to the antibody. Hence, samples with different concentrations were introduced to different sensing groups rather than successively introduced to a single group. The reaction time of each sample is 10 min with a flow rate of 5 ll/min. In order to remove the unbound antigen and maintain the refractive index of the aqueous cladding layer consistent with its initial state, we washed the sensing surface with PBS solution for 5 min at 10 ll/min. The real-time response of the SUMIRR-based biosensor to a specific concentration of SARS-CoV-2 antigen is shown in Fig. 6(b). It should be noted that the time resolution of the system is limited to a certain extent by the OSA and serial communication speed, resulting in a data refresh time of 6 s. Nonetheless, this limitation is acceptable in the actual testing process, as the primary focus is on the redshift observed when reactions conclude. Furthermore, we analyzed the peak shift for each concentration before and after washing [Fig. 6(c)]. The concentration-dependent response after washing fits well with the

Hill model, as demonstrated in Fig. 6(d).<sup>65,66</sup> The results further support a positive concentration-dependent correlation, with an antigen concentration 200 fg/ml can induce a remarkable response much higher than noise level.

# C. Specificity analysis and concurrent detection

This study aimed to achieve the concurrent detection of SARS-CoV-2 and influenza virus, requiring separate functionalization of two sensing groups. Specifically, the SARS-CoV-2 spike antibody and pan influenza A nucleoprotein antibody were introduced from the left port and right port surface for functionalization, <sup>67</sup> respectively, while the common port served as the inlet during testing [Fig. S12(b)]. Before demonstrating the concurrent detection, we first examined the specificity of the optical assay based on antibody-antigen combination. Samples containing influenza nucleoprotein and SARS-CoV-2 spike protein were successively introduced into the sensing group functionalized by SARS-CoV-2 spike antibody, and the verification for influenza nucleoprotein antibody was conducted using the same logic. The flow rate and reaction time for each step were consistent with those in Sec. IV B. In addition, according to the antigen concentration in nasopharyngeal swab specimens from COVID-19 patients, we selected 100 pg/ml as the antigen concentration for this experiment.<sup>23</sup> As shown in Figs. 7(a) and 7(b), the optical assay shows a clear signal difference between positive and negative. However, a slight shift (A5 pm) is observed for antigens that do not match the antibody, which may result from nonspecific interactions or incomplete BSA blocking. This undesired response necessitates more careful

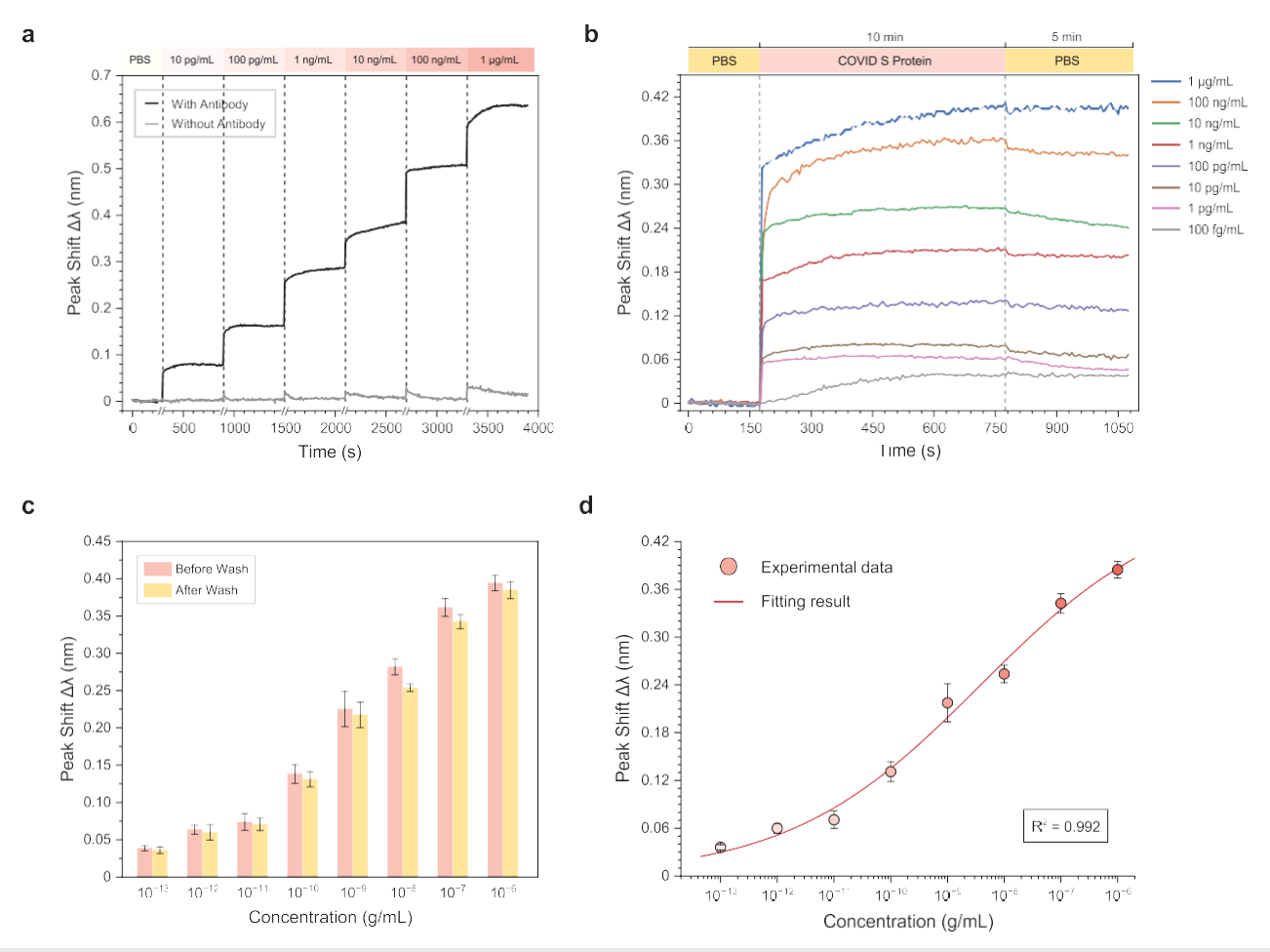


FIG. 6. Real-time detection of SARS-CoV-2 antigen. (a) Real-time response of the SUMIRR-based biosensor to SARS-CoV-2 spike protein was introduced successively in ascending order of concentration. The gray line represents the negative control group without anti-S protein antibody coating. The interval for sample replacement and PBS washing is not shown in the figure, resulting in step changes. (b) Real-time response of the SUMIRR biosensor to a specific concentration of SARS-CoV-2 spike protein. (c) Resonant peak shifts due to spike protein with varying concentrations before and after PBS washing. (d) Concentration-dependent response curve based on the peak shifts after PBS washing (details of the curve fitting are given in the supplementary material).

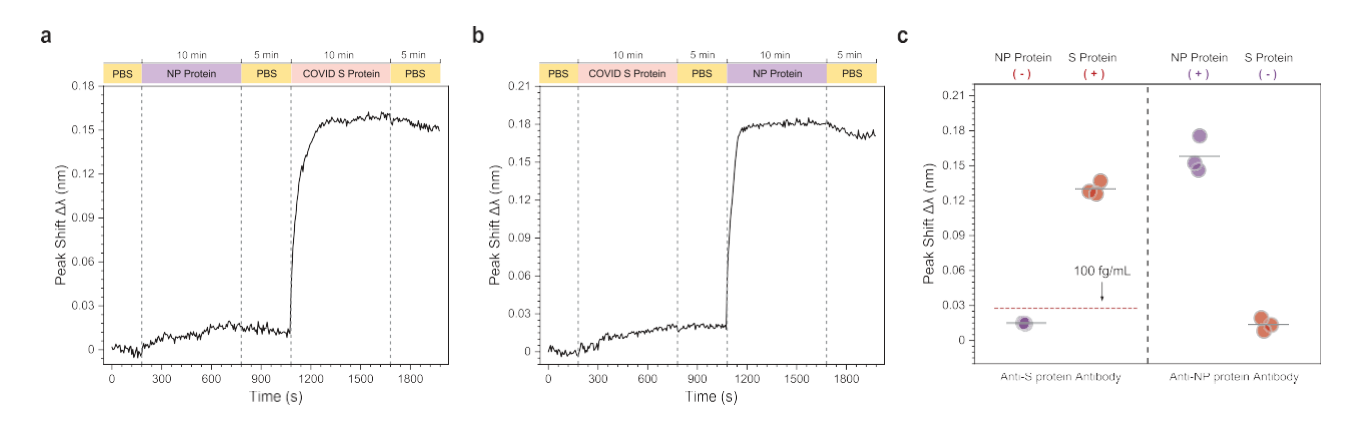


FIG. 7. Concurrent detection for SARS-CoV-2 spike protein and influenza nucleoprotein. (a) and (b) Specific response of SUMIRR biosensor to different antigens. The real-time responses shown in (a) and (b) were obtained from the sensing groups functionalized by SARS-CoV-2 and influenza antibodies, respectively. (c) Cross-reactivity tests for SARS-CoV-2 and influenza. Samples that contain SARS-CoV-2 spike protein/influenza nucleoprotein test positive for the corresponding antibody while negative for the other antibody.

determination of the LOD of sensing system. The concurrent detection results further indicate the specificity of antibody—antigen combination [Fig. 7(c)]. In addition, SARS-CoV-2 spike protein samples with concentrations above 100 fg/mL induce significant peak shifts, clearly distinguishable from nonspecific responses. Therefore, taking 100 fg/ml as the LOD of system is conservative and reliable.

#### V. DISCUSSION AND CONCLUSIONS

In this study, we have developed a POC biosensor that enables concurrent detection and differentiation of two analytes using SUMIRRs. The integration of a microfluidic chip and advanced packaging enhances the convenience of the sensing unit for clinical tests and improves reliability. The antibody immobilized on SUMIRRs induces resonant peak shifts upon binding with the antigen in sample. By analyzing the redshift, we have demonstrated the ability to quantitatively detect the concentration of SARS-CoV-2 spike protein with a LOD of 100 fg/ml. Moreover, cross-validation of SARS-CoV-2/influenza antigens and their corresponding antibodies indicates the high specificity of the optical assay based on antibody–antigen interactions.

One limitation of our study is that the current experiments focus on the quantitative testing of simplified samples due to the difficulty in acquiring real patient samples. Future work can be directed toward demonstrating sensing performance with complex human samples, such as nasopharyngeal swabs, saliva, or blood samples stored or diluted with specific buffers. However, since the SUMIRR-based biosensor is sensitive to the refractive index near the sensing surface and is independent of other solution properties, different buffers should not significantly impact the sensing performance. In addition, the high sensitivity and specificity achieved with samples containing a wide range of analyte loads further suggest that our SUMIRR-based sensing platform could offer a faster, simpler, and noninvasive alternative to RT-PCR and other POC diagnostics.

To facilitate clinical POC testing, we aim to further simplify the packaging process and improve system reliability. We are developing a portable system based on this technology that integrates a PC, syringe pump, light source, OSA, and software. In addition, an automatic optical alignment module has also been designed to reduce labor costs. Similarly, transitioning to injection molding techniques for the 3D-printed holder and microfluidic chips will allow for large-scale production, while pre-functionalized photonic integrated circuit chips can be lyophilized and sealed for streamlined assay use.

The COVID-19 pandemic has underscored the urgent need for rapid testing and differentiation of infections with similar symptoms. Our SUMIRR-based LOC biosensor for the quantitative detection of multiple analytes provides a promising solution to overcome the challenge and promotes the development of POC diagnostic tools.

#### SUPPLEMENTARY MATERIAL

See the supplementary material for the illustrations of system setup, summary of COVID-19 detection techniques, details regarding simulation and optimization, information about the peak tracking algorithm, improvement for POC testing, and supporting information related to experiments.

#### ACKNOWLEDGMENTS

This research program was supported by Omega Optics, National Institutes of Health on biomarker detection (No. HHSN261201200043C), Air Force Office of Scientific ResearchMultidisciplinary Research Program of the University Research Initiative (MURI) on silicon nanomembrane devices (No. AF9550-08-1-0394), and National Science Foundation on Fourier Transform Spectroscopy Sensor (NSF Award No. 1932753) and the Texas State Endowment from the University of Texas, Austin. The authors wish to acknowledge Dr. Chao Wang for his help in this study.

#### **AUTHOR DECLARATIONS**

#### Conflict of Interest

The authors have no conflicts to disclose.

# **Author Contributions**

Shupeng Ning: Conceptualization (equal); Formal analysis (lead); Investigation (lead); Methodology (lead); Visualization (lead); Writing – original draft (lead). Hao-Chen Chang: Formal analysis (supporting); Methodology (supporting); Resources (lead); Supervision (supporting). Kang-Chieh Fan: Software (lead). Po-yu Hsiao: Investigation (supporting); Methodology (supporting); Chenghao Feng: Investigation (supporting); Methodology (supporting); Validation (lead). Devan Shoemaker: Methodology (supporting). Ray T. Chen: Conceptualization (equal); Funding acquisition (lead); Project administration (lead); Supervision (lead); Writing – review & editing (lead).

#### DATA AVAILABILITY

The data that support the findings of this study are available within the article and its supplementary material.

## **REFERENCES**

- <sup>1</sup>S. Zhao, Q. Lin, J. Ran, S. S. Musa, G. Yang, W. Wang, Y. Lou, D. Gao, L. Yang, and D. He, "Preliminary estimation of the basic reproduction number of novel coronavirus (2019-nCoV) in China, from 2019 to 2020: A data-driven analysis in the early phase of the outbreak," Int. J. Infect. Dis. 92, 214–217 (2020).
- <sup>2</sup>L.-L. Ren, Y.-M. Wang, Z.-Q. Wu, Z.-C. Xiang, L. Guo, T. Xu, Y.-Z. Jiang, Y. Xiong, Y.-J. Li, and X.-W. Li, "Identification of a novel coronavirus causing severe pneumonia in human: A descriptive study," Chin. Med. J. 133(09), 1015–1024 (2020).
- <sup>3</sup>M. Khan, S. F. Adil, H. Z. Alkhathlan, M. N. Tahir, S. Saif, M. Khan, and S. T. Khan, "COVID-19: A global challenge with old history, epidemiology and progress so far," Mol 26(1), 39 (2020).
- <sup>4</sup>World Health Organization, see <a href="https://covid19.who.int/">https://covid19.who.int/</a> for "WHO Coronavirus (COVID-19) Dashboard" (accessed November 15, 2022).
- <sup>5</sup>D. Tian, Y. Sun, J. Zhou, and Q. Ye, "The global epidemic of SARS-CoV-2 variants and their mutational immune escape," J. Med. Virol. 94(3), 847–857 (2022).
- <sup>6</sup>J. A. Sheikh, J. Singh, H. Singh, S. Jamal, M. Khubaib, S. Kohli, U. Dobrindt, S. A. Rahman, N. Z. Ehtesham, and S. E. Hasnain, "Emerging genetic diversity among clinical isolates of SARS-CoV-2: Lessons for today," Infect., Genet. Evol. 84, 104330 (2020).
- <sup>7</sup>M. Giovanetti, F. Benedetti, G. Campisi, A. Ciccozzi, S. Fabris, G. Ceccarelli, V. Tambone, A. Caruso, S. Angeletti, and D. Zella, "Evolution patterns of SARS-CoV-2: Snapshot on its genome variants," Biochem. Biophys. Res. Commun. 538, 88–91 (2021).
- <sup>8</sup>W. T. Harvey, A. M. Carabelli, B. Jackson, R. K. Gupta, E. C. Thomson, E. M. Harrison, C. Ludden, R. Reeve, A. Rambaut, and S. J. Peacock, "SARS-CoV-2 variants, spike mutations and immune escape," Nat. Rev. Microbiol. 19(7), 409–424 (2021).
- <sup>9</sup>P. Fathi-Hafshejani, N. Azam, L. Wang, M. A. Kuroda, M. C. Hamilton, S. Hasim, and M. Mahjouri-Samani, "Two-dimensional-material-based field-

- effect transistor biosensor for detecting COVID-19 virus (SARS-CoV-2)," ACS Nano 15(7), 11461–11469 (2021).
- <sup>10</sup>A. Asghari, C. Wang, K. M. Yoo, A. Rostamian, X. Xu, J.-D. Shin, H. Dalir, and R. T. Chen, "Fast, accurate, point-of-care COVID-19 pandemic diagnosis enabled through advanced lab-on-chip optical biosensors: Opportunities and challenges," Appl. Phys. Rev. 8(3), 031313 (2021).
- <sup>11</sup>D. Tian, Y. Sun, H. Xu, and Q. Ye, "The emergence and epidemic characteristics of the highly mutated SARS-CoV-2 Omicron variant," J. Med. Virol. 94(6), 2376–2383 (2022).
- <sup>12</sup>C. Maslo, R. Friedland, M. Toubkin, A. Laubscher, T. Akaloo, and B. Kama, "Characteristics and outcomes of hospitalized patients in South Africa during the COVID-19 Omicron wave compared with previous waves," J. Am. Med. Assoc. 327(6), 583–584 (2022).
- <sup>13</sup>P. A. Christensen, R. J. Olsen, S. W. Long, R. Snehal, J. J. Davis, M. O. Saavedra, K. Reppond, M. N. Shyer, J. Cambric, and R. Gadd, "Signals of significantly increased vaccine breakthrough, decreased hospitalization rates, and less severe disease in patients with Coronavirus disease 2019 caused by the Omicron variant of severe acute respiratory syndrome Coronavirus 2 in Houston, Texas," Am. J. Pathol. 192(4), 642–652 (2022).
- <sup>14</sup>H. Khorramdelazad, M. H. Kazemi, A. Najafi, M. Keykhaee, R. Z. Emameh, and R. Falak, "Immunopathological similarities between COVID-19 and influenza: Investigating the consequences of Co-infection," Microb. Pathog. 152, 104554 (2021).
- <sup>15</sup>A. Pormohammad, S. Ghorbani, A. Khatami, M. H. Razizadeh, E. Alborzi, M. Zarei, J. P. Idrovo, and R. J. Turner, "Comparison of influenza type A and B with COVID-19: A global systematic review and meta-analysis on clinical, laboratory and radiographic findings," Rev. Med. Virol. 31(3), e2179 (2021).
- <sup>16</sup>A. S. Monto, S. Gravenstein, M. Elliott, M. Colopy, and J. Schweinle, "Clinical signs and symptoms predicting influenza infection," Arch. Intern. Med. 160(21), 3243–3247 (2000).
- <sup>17</sup>Y. Liu and J. Rocklóv, "The effective reproduction number for the omicron SARS-CoV-2 variant of concern is several times higher than Delta," J. Travel Med. 12(3), taac037 (2022).
- <sup>18</sup>A. Tahamtan and A. Ardebili, "Real-time RT-PCR in COVID-19 detection: Issues affecting the results," Expert Rev. Mol. Diagn. 20(5), 453–454 (2020).
- <sup>19</sup>W. M. Freeman, S. J. Walker, and K. E. Vrana, "Quantitative RT-PCR: Pitfalls and potential," <u>Biotechniques</u> 26(1), 112–125 (1999).
- <sup>20</sup>U. É. Gibson, C. A. Heid, and P. M. Williams, "A novel method for real time quantitative RT-PCR," Genome Res. 6(10), 995–1001 (1996).
- <sup>21</sup>C. Wang, C. Wang, X. Wang, K. Wang, Y. Zhu, Z. Rong, W. Wang, R. Xiao, and S. Wang, "Magnetic SERS strip for sensitive and simultaneous detection of respiratory viruses," ACS Appl. Mater. Interfaces 11(21), 19495–19505 (2019).
- <sup>22</sup>D. Najjar, J. Rainbow, S. Sharma Timilsina, P. Jolly, H. De Puig, M. Yafia, N. Durr, H. Sallum, G. Alter, and J. Z. Li, "A lab-on-a-chip for the concurrent electrochemical detection of SARS-CoV-2 RNA and anti-SARS-CoV-2 anti-bodies in saliva and plasma," Nat. Biomed. Eng. 6(8), 968–978 (2022).
- <sup>23</sup>G. Seo, G. Lee, M. J. Kim, S.-H. Baek, M. Choi, K. B. Ku, C.-S. Lee, S. Jun, D. Park, and H. G. Kim, "Rapid detection of COVID-19 causative virus (SARS-CoV-2) in human nasopharyngeal swab specimens using field-effect transistor-based biosensor," ACS Nano 14(4), 5135–5142 (2020).
- <sup>24</sup>S. M. Yoo and S. Y. Lee, "Optical biosensors for the detection of pathogenic microorganisms," Trends Biotechnol. 34(1), 7–25 (2016).
- <sup>25</sup>E. Luan, H. Shoman, D. M. Ratner, K. C. Cheung, and L. Chrostowski, "Silicon photonic biosensors using label-free detection," Sensors 18(10), 3519 (2018).
- <sup>26</sup>Z. Liao, Y. Zhang, Y. Li, Y. Miao, S. Gao, F. Lin, Y. Deng, and L. Geng, "Microfluidic chip coupled with optical biosensors for simultaneous detection of multiple analytes: A review," Biosens. Bioelectron. 126, 697–706 (2019).
- <sup>27</sup>K. M. Yoo and R. T. Chen, "Monolithic integration of Si<sub>3</sub>N<sub>4</sub> ring resonator and on-chip Fourier transform spectrometer for the lab-on-a-chip biosensor," in *Conference on Lasers and Electro-Optics* (IEEE, 2022).
- <sup>28</sup>C.-J. Yang, H. Yan, N. Tang, Y. Zou, Y. Al-Hadeethi, X. Xu, H. Dalir, and R. T. Chen, "Ultra sensitivity silicon-based photonic crystal microcavity biosensors for plasma protein detection in patients with pancreatic cancer," Micromachines 11(3), 282 (2020).
- <sup>29</sup>J. S. Cognetti, M. T. Moen, M. G. Brewer, M. R. Bryan, J. D. Tice, J. L. McGrath, and B. L. Miller, "A photonic biosensor-integrated tissue chip

- platform for real-time sensing of lung epithelial inflammatory markers," Lab Chip 23, 239–250 (2023).
- <sup>30</sup>M. R. Bryan, J. N. Butt, J. Bucukovski, and B. L. Miller, "Biosensing with silicon nitride microring resonators integrated with an on-chip filter bank spectrometer," ACS Sensors 8(2), 739–747 (2023).
- <sup>31</sup>E. Aljohani, S. Gundavarapu, C. A. Chapman, C.-C. Lin, and D. Vermeulen, "Foundry compatible fabrication of Si<sub>3</sub>N<sub>4</sub> microring resonators for 15-plex biosensing at 1310 nm," Proc. SPIE 12006, 120060F (2022).
- <sup>32</sup>J. Arlett, E. Myers, and M. Roukes, "Comparative advantages of mechanical biosensors," Nat. Nanotechnol. 6(4), 203–215 (2011).
- <sup>33</sup>H. Yan, L. Huang, X. Xu, S. Chakravarty, N. Tang, H. Tian, and R. T. Chen, "Unique surface sensing property and enhanced sensitivity in microring resonator biosensors based on subwavelength grating waveguides," Opt. Express 24(26), 29724–29733 (2016).
- <sup>34</sup>Z. Wang, X. Xu, D. Fan, Y. Wang, and R. T. Chen, "High quality factor subwavelength grating waveguide micro-ring resonator based on trapezoidal silicon pillars," Opt. Lett. 41(14), 3375–3378 (2016).
- <sup>35</sup>S. Schmidt, J. Flueckiger, W. Wu, S. M. Grist, S. T. Fard, V. Donzella, P. Khumwan, E. R. Thompson, Q. Wang, and P. Kulik, 2014. "Improving the performance of silicon photonic rings, disks, and Bragg gratings for use in label-free biosensing," *Biosensing and Nanomedicine VII*, pp. 71–108. SPIE.
- <sup>36</sup>X. Xu, Z. Pan, C.-J. Chung, C.-W. Chang, H. Yan, and R. T. Chen, "Subwavelength grating metamaterial racetrack resonator for sensing and modulation," IEEE J. Sel. Top. Quantum Electron. 25(3), 1–8 (2019).
- <sup>37</sup>Z. Wang, H. Yan, S. Chakravarty, H. Subbaraman, X. Xu, D. Fan, A. X. Wang, and R. T. Chen, "Microfluidic channels with ultralow-loss waveguide crossings for various chip-integrated photonic sensors," Opt. Lett. 40(7), 1563–1566 (2015).
- <sup>38</sup>V. Soni, C.-W. Chang, X. Xu, C. Wang, H. Yan, M. D'Agati, L.-W. Tu, Q. Y. Chen, H. Tian, and R. T. Chen, "Portable automatic microring resonator system using a subwavelength grating metamaterial waveguide for high-sensitivity real-time optical-biosensing applications," IEEE Trans. Biomed. Eng. 68(6), 1894–1902 (2020).
- <sup>39</sup>S. Ning, S. Liu, Y. Xiao, G. Zhang, W. Cui, and M. Reed, "A microfluidic chip with a serpentine channel enabling high-throughput cell separation using surface acoustic waves," Lab Chip 21(23), 4608–4617 (2021).
- <sup>40</sup>V. Donzella, A. Sherwali, J. Flueckiger, S. M. Grist, S. T. Fard, and L. Chrostowski, "Design and fabrication of SOI micro-ring resonators based on sub-wavelength grating waveguides," Opt. Express 23(4), 4791–4803 (2015).
- <sup>41</sup>E. Luan, H. Yun, L. Laplatine, Y. Dattner, D. M. Ratner, K. C. Cheung, and L. Chrostowski, "Enhanced sensitivity of subwavelength multibox waveguide microring resonator label-free biosensors," IEEE J. Sel. Top. Quantum Electron. 25(3), 1–11 (2018).
- <sup>42</sup>N. A. Yebo, D. Taillaert, J. Roels, D. Lahem, M. Debliquy, D. Van Thourhout, and R. Baets, "Silicon-on-insulator (SOI) ring resonator-based integrated optical hydrogen sensor," IEEE Photonics Technol. Lett. 21(14), 960–962 (2009).
- <sup>43</sup>R. Halir, P. J. Bock, P. Cheben, A. Ortega-Monux, C. Alonso-Ramos, J. H. Schmid, J. Lapointe, D. X. Xu, J. G. Wangüemert-Pérez, and Í. Molina-Fernández, "Waveguide sub-wavelength structures: A review of principles and applications," Laser Photonics Rev. 9(1), 25–49 (2015).
- <sup>44</sup>Z. Wang, X. Xu, D. Fan, Y. Wang, H. Subbaraman, and R. T. Chen, "Geometrical tuning art for entirely subwavelength grating waveguide based integrated photonics circuits," Sci. Rep. 6(1), 24106 (2016).
- <sup>45</sup>T. Taniguchi, A. Hirowatari, T. Ikeda, M. Fukuyama, Y. Amemiya, A. Kuroda, and S. Yokoyama, "Detection of antibody-antigen reaction by silicon nitride slot-ring biosensors using protein G," Opt. Commun. 365, 16–23 (2016).
- <sup>46</sup>S. Yousuf, J. Kim, A. Orozaliev, M. S. Dahlem, Y.-A. Song, and J. Viegas, "Label-free detection of morpholino-DNA hybridization using a silicon photonics suspended slab micro-ring resonator," IEEE Photonics J. 13(4), 1–9 (2021).
- <sup>47</sup>J. D. Jackson, Classical Electrodynamics (American Association of Physics Teachers, 1999).
- 48P. Steglich, M. H\u00edlsemann, B. Dietzel, and A. Mai, "Optical biosensors based on silicon-on-insulator ring resonators: A review," Molecules 24(3), 519 (2019).
- <sup>49</sup>L. Chrostowski, S. Grist, J. Flueckiger, W. Shi, X. Wang, E. Ouellet, H. Yun, M. Webb, B. Nie, and Z. Liang, "Silicon photonic resonator sensors and devices,"

- in Laser Resonators, Microresonators, and Beam Control XIV (SPIE, 2012), pp. 387-402.
- <sup>50</sup>Y. R. Bawankar and A. Singh, "Microring resonators based applications in silicon Photonics-A review," in *Fifth International Conference on Computational Intelligence and Communication Technologies (CCICT)* (IEEE, 2021).
- <sup>51</sup>J. Ackert, J. Doylend, D. Logan, P. Jessop, R. Vafaei, L. Chrostowski, and A. Knights, "Defect-mediated resonance shift of silicon-on-insulator racetrack resonators," Opt. Express 19(13), 11969–11976 (2011).
- <sup>52</sup>S. T. Fard, V. Donzella, S. A. Schmidt, J. Flueckiger, S. M. Grist, P. T. Fard, Y. Wu, R. J. Bojko, E. Kwok, and N. A. Jaeger, "Performance of ultra-thin SOI-based resonators for sensing applications," Opt. Express 22(12), 14166–14179 (2014).
- <sup>53</sup>Y. Xia and G. M. Whitesides, "Soft lithography," Angew. Chem., Int. Ed 37(5), 550–575 (1998).
- <sup>54</sup>E. Kim, M. S. Khan, A. Ferrari, S. Huang, J. C. Sammartino, E. Percivalle, T. W. Kenniston, I. Cassaniti, F. Baldanti, and A. Gambotto, "SARS-CoV-2 S1 subunit booster vaccination elicits robust humoral immune responses in aged mice," bioRxiv (2022).
- <sup>55</sup>A. L. Ahmad, T. A. Otitoju, and B. S. Ooi, "Optimization of a high performance 3-aminopropyltriethoxysilane-silica impregnated polyethersulfone membrane using response surface methodology for ultrafiltration of synthetic oil-water emulsion," J. Taiwan Inst. Chem. Eng. 93, 461–476 (2018).
- <sup>56</sup>S. Udomsom, U. Mankong, P. Paengnakorn, and N. Theera-Umpon, "Novel rapid protein coating technique for silicon photonic biosensor to improve surface morphology and increase bioreceptor density," Coatings 11(5), 595 (2021).
- <sup>57</sup>H. M. Robison and R. C. Bailey, "A guide to quantitative biomarker assay development using whispering gallery mode biosensors," Curr. Protoc. Chem. Biol. 9(3), 158–173 (2017).
- <sup>58</sup>A. J. Qavi, K. Meserve, M. J. Aman, H. Vu, L. Zeitlin, J. M. Dye, J. W. Froude, D. W. Leung, L. Yang, and F. W. Holtsberg, "Rapid detection of an Ebola biomarker with optical microring resonators," Cells Rep. Methods 2, 100234 (2022).

- <sup>59</sup>C.-W. Chang, X. Xu, S. Chakravarty, H.-C. Huang, L.-W. Tu, Q. Y. Chen, H. Dalir, M. A. Krainak, and R. T. Chen, "Pedestal subwavelength grating metamaterial waveguide ring resonator for ultra-sensitive label-free biosensing," Biosens. Bioelectron. 141, 111396 (2019).
- <sup>60</sup>M. Lahav, A. Vaskevich, and I. Rubinstein, "Biological sensing using transmission surface plasmon resonance spectroscopy," Langmuir 20(18), 7365–7367 (2004)
- <sup>61</sup>R. Janeiro, R. Flores, and J. Viegas, "Refractive index of phosphate-buffered saline in the telecom infrared CpL bands," OSA Continuum 4(12), 3039–3051 (2021)
- <sup>62</sup>R. Lu, X. Zhao, J. Li, P. Niu, B. Yang, H. Wu, W. Wang, H. Song, B. Huang, and N. Zhu, "Genomic characterisation and epidemiology of 2019 novel coronavirus: Implications for virus origins and receptor binding," Lancet 395(10224), 565–574 (2020).
- <sup>63</sup>Y. Shi, Y. Wang, C. Shao, J. Huang, J. Gan, X. Huang, E. Bucci, M. Piacentini, G. Ippolito, and G. Melino, "COVID-19 infection: The perspectives on immune responses," Cell Death Differ. 27(5), 1451–1454 (2020).
- <sup>64</sup>G. Zhou and Q. Zhao, "Perspectives on therapeutic neutralizing antibodies against the Novel Coronavirus SARS-CoV-2," Int. J. Biol. Sci. 16(10), 1718– 1723 (2020).
- <sup>65</sup>C. Ligiero, T. Fernandes, D. D'Amato, F. Gaspar, P. Duarte, M. Strauch, J. Fonseca, L. Meirelles, P. B. da Silva, and R. Azevedo, "Influence of particle size on the SARS-CoV-2 spike protein detection using IgG-capped gold nanoparticles and dynamic light scattering," Mater. Today Chem. 25, 100924 (2022).
- <sup>66</sup>G. Ruiz, N. Ryan, K. Rutschke, O. Awotunde, and J. D. Driskell, "Antibodies irreversibly adsorb to gold nanoparticles and resist displacement by common blood proteins," Langmuir 35(32), 10601–10609 (2019).
- <sup>67</sup>K. Leirs, P. Tewari Kumar, D. Decrop, E. Pérez-Ruiz, P. Leblebici, B. Van Kelst, G. Compernolle, H. Meeuws, L. Van Wesenbeeck, and O. Lagatie, "Bioassay development for ultrasensitive detection of influenza a nucleoprotein using digital ELISA," Anal. Chem. 88(17), 8450–8458 (2016).